Solute Transport in Growth Plate Cartilage: In Vitro and In Vivo

Rebecca M. Williams,* Warren R. Zipfel,† Michelle L. Tinsley,‡ and Cornelia E. Farnum‡
*Applied and Engineering Physics, †Biomedical Engineering, and ‡Biomedical Sciences, Cornell University, Ithaca, New York

ABSTRACT Bone elongation originates from cartilaginous discs (growth plates) at both ends of a growing bone. Here chondrocytes proliferate and subsequently enlarge (hypertrophy), laying down a matrix that serves as the scaffolding for subsequent bone matrix deposition. Because cartilage is generally avascular, all nutrients, oxygen, signaling molecules, and waste must be transported relatively long distances through the tissue for it to survive and function. Here we examine the transport properties of growth plate cartilage. Ex vivo, fluorescence photobleaching recovery methods are used in tissue explants. In vivo, multiphoton microscopy is used to image through an intact perichondrium and into the cartilage of anesthetized mice. Systemically introduced fluorescent tracers are monitored directly as they move from the vasculature into the cartilage. We demonstrate the existence of a relatively permissive region at the midplane of the growth plate, where chondrocytes transition from late proliferative to early hypertrophic stages and where paracrine communication is known to occur between chondrocytes and cells in the surrounding perichondrium. Transport in the living mouse is also significantly affected by fluid flow from the two chondro-osseus junctions, presumably resulting from a pressure difference between the bone vasculature and the cartilage.

INTRODUCTION

Bone elongation occurs by endochondral ossification, which is controlled at the cellular level by chondrocytes within the growth plate (Fig. 1). These cells undergo a differentiation cascade in which stem cells (resting cells) at the epiphyseal (*E*) side first undergo a proliferation phase, followed by a hypertrophy phase in which they stop dividing, enlarge and lay down an extracellular scaffolding for new bone formation at the metaphyseal (*M*) side (toward the diaphysis). The extent of chondrocytic enlargement can be directly correlated to the extent of bone elongation (1–3). After death of the terminal chondrocyte, the replacement of cartilage by bone occurs via a synchronized interaction among endothelial cells, chondroclasts, and bone precursor cells. Chondrocytic activity in the growth plate is regulated by a wide array of autocrine and paracrine regulators (for reviews, see 4–9), many of which are produced at sites distant from their sites of action. A clearly demonstrated example is the PTHrP/Ihh signaling loop in which parathyroid-related protein (PTHrP) produced within the periarticular chondrocytes and perichondrium is known to limit the number of chondrocytes that express Indian Hedgehog (Ihh). In addition to inducing chondrocytes to begin differentiation, Ihh also acts to upregulate PTHrP expression, completing a negative feedback loop that delays the rate of overall chondrocyte differentiation (10,11).

The mechanism by which remotely produced signals maintain such a tight regulation remains unclear, especially in the postnatal animal. Other examples of remotely produced diffusible effector molecules with action on the chondrogenic differentiation cascade within the growth plate include fibroblast growth factor 18, various isoforms of bone morphogenic protein (BMPs), and transforming growth factor-beta, which all are produced in the cambrial layer of the perichondrium surrounding the growth plate (4,6,9,12). Analogously, matrix metalloproteases (MMPs MMP-9 and MT-MMP) produced by chondroclasts at the metaphyseal chondro-osseus junction (COJ) are essential for apoptosis of terminal hypertrophic chondrocytes and subsequent vessel invasion and bone formation (13–16). The spatial location of the signals produced and the transport properties of the cartilage are critical to the communication between cells and the maintenance of growth plate organization. A particularly elegant demonstration comes from a comprehensive examination of the signaling defects in the skeletal disorder Exostosin1 (EXT1) mutation. EXT1 mutations result in a loss of heparin sulfate chains on extracellular matrix (ECM) proteoglycans, which dramatically decreases the interaction of Ihh with the ECM, increasing the range of Ihh signaling within the growth plate and causing an extended proliferative zone due to excessive activation of PTHrP (17–19). Note that the phenotype originates from a defect to the transport properties of the signaling molecule, rather than to the molecule itself. In humans, these mutations result in a variety of skeletal abnormalities such as bone deformities, joint fusions, and short stature. The diffusible range of a particular effector molecule or morphogen is a concept that is generally ubiquitous to the literature of development and developmental processes (for example, see (20)).

The transport properties of growth plate cartilage are crucial not only to understanding molecular signaling, but to understanding chondrocytic viability generally. Several decades ago, it was shown that growth plate chondrocytes at all stages of differentiation die after compromising the epiphyseal vasculature (21). The paradigm that chondrocyte viability is dependent upon a viable epiphyseal vasculature remains true today (for example, see (22)). By contrast, a compromise to the metaphyseal vasculature does not result in chondrocytic

Submitted September 18, 2006, and accepted for publication March 30, 2007.

Address reprint requests to R. M. Williams, Tel.: 607-255-8034; E-mail: rw36@cornell.edu.

Editor: Elliot L. Elson.

0006-3495/07/08/1039/12 $2.00

doi: 10.1529/biophysj.106.097675

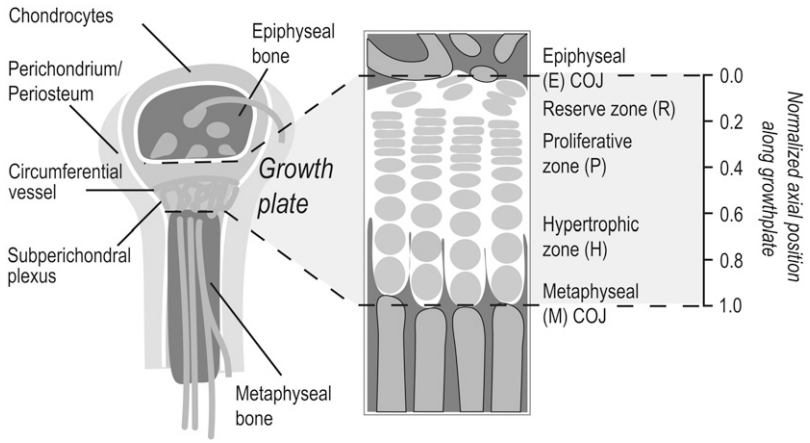

FIGURE 1 Diagram of a juvenile bone, showing the three major vascular sources to the avascular growth plate. Chondrocytes align in axial rows and proliferate extensively. Differentiation and hypertrophy of these cells is thought to be involved in the pushing of the epiphysis away from the elongating metaphysis. Secreted matrix acts as the scaffolding for bone formation at the metaphyseal end. Spatially varying transport coefficients are described in terms of the normalized axial position from 0.0 at the epiphyseal COJ to 1.0 at the metaphyseal COJ. Note that the proliferative-to-hypertrophic transition occurs roughly at the axial center of the growth plate.

death within the growth plate (21), only a failure of chondrocytic apoptosis and bone formation on the metaphyseal side. Taken together, these findings have led to a hypothesized unidirectional entrance of nutrients, sourced by the epiphyseal vasculature. In addition, a somewhat controversial hypothesis (23) states that hypertrophic chondrocytes are hypoxic, driven by the fact that angiogenesis in the hypertrophic zone (and chondrocytic differentiation generally) is regulated by hypoxia inducible transcription factor 1α (HIF-1α (24)). These ideas suggest that chondrocytic access to oxygen and nutrients from the metaphyseal vasculature is somewhat limited, even though the vessels at this location are known to be leaky (25), as is characteristic of actively growing and remodeling vasculature.

The goal of this investigation was to understand the biophysical properties of molecular transport in and around the growth plate using several strategies. Firstly, ex vivo analyses were carried out in coarse-cut growth plate sections using a three-dimensionally resolved form of fluorescence photobleaching recovery (26,27). Secondly, fluorescent tracers were introduced into the systematic vasculature of anesthetized animals and their arrival into the growth plate, imaged directly using multiphoton microscopy (28). This technique allowed us to image through the intact perichondrium, which is highly vascularized and critical to growth plate function. Tracers entered into the growth plate from three sources: bone vasculature on the epiphyseal side, bone vasculature on the metaphyseal side, and a vascular plexus surrounding the growth plate just deep to the perichondrium (Fig. 1). Previously we have shown that equilibration into the growth plate took several minutes (29). In the present study, fluorescence entry curves were fit to determine flow rates and diffusion coefficients within the cartilage. Both ex vivo and in vivo strategies revealed a permissive region at the midplane of the growth plate, where chondrocytes make an abrupt transition from a proliferative (*P*) to a hypertrophic (*H*) phenotype. Regions adjacent to the two chondro-osseus junctions were severalfold more hindered to diffusion. Flow from the bone into the cartilage also enhanced equilibration of small vascular solutes into the growth plate.

MATERIALS AND METHODS

We chose two methods for examining the transport properties of growth plate cartilage. Both require multiphoton microscopy for sectioning relatively deeply into tissue. In the first ex vivo method, we measured the diffusion coefficient in isolated cartilage by focusing the beam to a micron-sized spot in the extracellular matrix, photobleaching the fluorescent tracers in that spot and monitoring the recovery to determine the diffusion coefficient. In the second in vivo method, a surgical approach was made to the proximal tibia in an anesthetized mouse. We imaged through the perichondrium and in to the growth plate to determine how a bolus of tracer injected into the bloodstream moves into the growth plate. The second method resulted in a time series of images of tracer entering from the bloodstream and equilibrating through the growth plate in a live animal. This method allowed us to examine general theories such as the hypothesized epiphyseal sourcing of small solutes to the growth plate. Under defined conditions, image analysis methods could be used to determine transport coefficients in the living animal.

Multiphoton microscopy

We used a multiphoton microscope consisting of a Ti:Sapphire laser (Millennia Xs/Tsunami combination, Spectra Physics, Mountain View, CA) directed into a modified BioRad model No. MRC 600 laser scanner interfaced with a modified (fixed-stage) model No. AX-70 upright microscope (Olympus, Center Valley, PA). A model No. 350-80 BKLA Pockel's Cell (Conoptics, Danbury, CT) with custom-made electronics provided beam intensity modulation and blanking during scanner flyback. The excitation light was focused into the growth plate region with a large-barrel Olympus 20×/0.95 NA water objective, which provides a large field-of-view, a relatively high NA, good IR transmission, and the few mm of working distance essential for maneuvering in live animals.

As described previously (29), we oriented to the growth plate using collagen second-harmonic generation imaging of the perichondrial anatomy in addition to oxytetracycline (OTC) fluorescent labeling of the rapidly growing regions of bone directly adjacent to the growth plate. The multiphoton excitation wavelength peak (λ_{ex}) was tuned to 900 nm because FITC absorbs well at this wavelength (30), whereas water and intrinsic cellular absorbers do not (31). Nonlinear emissions were collected in epi mode and separated from the excitation beam directly after the objective with a model No. 670DCXXRU longpass dichroic (Chroma Technology, Rockingham). Emission filters were chosen for a blue (400–490 nm for collagen second-harmonic generation) and visible (510–650 nm for fluorescein and OTC emission) separation (model Nos. BGG22 and 580/150 filters with a separating model No. 500DCXR dichroic, Chroma Technology) and a 10^7 rejection ratio of the exciting to emitting wavelengths. The resulting two emissions were collected by model No. HC125-02 bialkali photomultiplier tube assemblies (Hamamatsu, Hamamatsu City, Japan) directed into the external ports of the BioRad acquisition electronics.

Fluorescent tracers

We used the fluorescent tracers fluorescein (FL, MW 332, AK-FLUOR, Akorn, Buffalo Grove, IL), 10 kDa fluorescein-labeled dextran (10k-FL, D1821, Invitrogen, Carlsbad, CA), 40 kDa fluorescein-labeled dextran (40k-FL, D-1844, Invitrogen), and a 45 kDa fluorescein-labeled ovalbumin (Ova-FL, O23020, Invitrogen) to mimic molecules across a range of molecular weights. Fluorescein was diluted 10-fold from 10% ophthalmologic stock solutions (300 mM) and a 50 μl intracardiac (IC) injection administered to yield an approximate vascular concentration of ~2 mM (for a typical 11 g mouse). Solutions of fluorescein-labeled dextrans were prepared at 100 mg/ml in phosphate-buffered saline solution. Depending on the labeling concentration, varying amounts were injected IC to yield a vascular fluorescence concentration similar to that for FL. For photobleaching analyses, coarsely-cut tibial sections were incubated in 100 μM equivalent dye.

Our goal was to use variously-sized neutral dextrans to mimic how variously-sized signaling molecules would be transported within the growth plate. However, we found that only the highly-anionic dextrans could be solubilized to the extent necessary for visualization in vivo. Thus, we could not separate charge-effects from size-effects for the larger tracers in the live animals.

Ex vivo diffusion coefficient measurement via photobleaching of isolated tissue

Specimens were prepared for ex vivo photobleaching analyses by halving isolated tibias from 4-to-5-week-old mice using a single cut with a razor head. These sections were immersed in lactated Ringer's solution with 5% fetal bovine serum and kept on ice for no more than 2 h. In isolated tissue slabs, we assume no flow, so that diffusion coefficients can be measured by a standard fluorescence photobleaching recovery (FPR) assay, in which a tightly focused beam is held stationary at the region of interest. A high-intensity laser pulse is used to bleach fluorophores within the focal volume. Subsequently at a lower monitoring intensity, the fluorescence increases due to fresh (unbleached) fluorophores back into the focal volume. This recovery is fit to determine a diffusion coefficient for this fluorescent species. (The technique is also known as fluorescence recovery after photobleaching or FRAP.) Multiphoton (MP) excitation is generally restricted to the focal volume, so that MP-FPR can be carried out in three dimensions rather than being limited to two dimensions as with standard (single photon) excitation (26,27).

For MP-FPR, we used the same scanning and detection instrumentation as described for multiphoton microscopy. We focused ~50 μm into the cartilage so as to measure far from the cut surface. The beam was then ''parked'' at a stationary location in the specimen and the Pockel's Cell was used to deliver repeated bleach pulses followed by monitoring periods with ~10-fold lower laser intensities. Fluorescence curves were acquired using a model No. SR430 multichannel scaler (Stanford Research Systems, Sunnyvale, CA) and the electronics were synchronized for repeated bleaching patterns using a model No. DG535 digital delay/pulse generator (Stanford Research Systems). The recovery curve (the postbleach fluorescence trace normalized to the initial fluorescence) was fit to the following numerical series for identifying two diffusion coefficients (26,27),

$$\frac{F(t)}{F_0} = A_1\left[\sum_{n=0}^{n\max}\frac{(-\beta)^n}{n!}\frac{1}{1+n+4nD_1t/w_r^2}\frac{1}{\sqrt{1+n+4nD_1t/w_z^2}}\right] + A_2\left[\sum_{n=0}^{n\max}\frac{(-\beta)^n}{n!}\frac{1}{1+n+4nD_2t/w_r^2}\frac{1}{\sqrt{1+n+4nD_2t/w_z^2}}\right], \quad (1)$$

where w_r and w_z are the $1/e^2$ lateral and axial radii of the two photon spot sizes (28) and β is the bleach depth. A_1 and A_2, the relative amplitudes of species diffusing with D_1 and D_2 diffusion coefficients, respectively, are determined using a three-parameter Marquardt-Levenberg algorithm ($A_1 + A_2 = 1$). Summation to $n = 10$ was usually sufficient for convergence. Critical to determining diffusive behavior accurately with this formulation are the assumptions that the bleach time is small compared to the recovery time and that the bleach depth is small compared to the total fluorescence (27). In an optical setup where the objective back aperture is overfilled by the laser beam (more precisely the $1/e$ width of the beam greater than the objective back aperture), the spot size is determined by the objective NA and exciting wavelength. We used excitation at 780 nm with an Olympus 20×/0.95NA water immersion objective, giving a w_r and w_z of 270 and 1040 nm, respectively (28). FPR measurements were carried out using a 50 μs bleach pulse with an intensity resulting in a bleach depth of <20%. The monitoring intensity was adjusted so as to not saturate the photon counter (<1 MHz count rates for the ~40 ns pulses emanating from the specified PMT module). Bleach and monitor powers at the specimen were measured to be 50–200 mW and 3–8 mW, respectively. Note that these powers were measured at the surface of the specimen and expected to be significantly lower at the imaging plane. Each measurement represents 5-μs binned data from ~100 repetitions at 10 Hz. Because recovery times are in the millisecond range, this frequency was low enough to ensure a complete recovery in the fluorescence curve before another bleach could occur.

Preparation of mice for in vivo imaging

Four-to-five-week-old C57BL/6 or DBA/2J mice were prepared for in vivo multiphoton imaging (29). The mouse to be imaged was injected 30 min before the imaging session with OTC (10 mg/kg intraperitoneal), which labels the chondro-osseous junctions with yellow-emitting fluorescence to aid in orientation for viewing. For surgery and imaging, the mouse was laid in dorsal recumbency on a temperature-regulated heating pad with its nose in an isoflurane gas anesthesia delivery tube. An incision was made on the posteriomedial aspect of the limb and overlying muscles were removed just caudal to the medial collateral ligament superficial to the proximal tibial growth plate. The limb was immobilized and immersed in Ringer's solution for imaging and the temperature of the bath maintained at 35°C with an inline solution heater (model No. TC344, Warner Instruments, Hamden, CT) and perfusion pumps (pump controller model No. T553-60, Masterflex, Gelsenkirchen, Germany). All procedures were approved by Cornell University's Institutional Animal Care and Use Committee.

In vivo diffusion coefficient measurement via elemental image analysis of tracer entry

The rate of exchange from the vasculature is dependent upon the pressure differential between the vasculature and the interstitial tissue. Within a living organism, transport properties are not necessarily diffusion-dominated. We observe tracer entering the growth plate from the vasculature and interpret the resulting images assuming that the tracer exhibits both diffusive and flow transport properties. The time rate of change of tracer concentration (C) undergoing Fickian (normal) diffusion with a spatially varying diffusion coefficient (D) and under a force-differential-causing flow is given by (32)

$$\frac{\partial C}{\partial t} = \nabla\cdot(D\nabla C) - \mathbf{v}\cdot\nabla C, \quad (2)$$

where D is the diffusion coefficient and $\mathbf{v}$ is the velocity of flow.

When focused deeply enough (>50 μm deep to the deep edge of the perichondrium), the subperichondrial ring vessel and plexus are negligible sources of tracer arrival to the growth plate (29). Under these conditions, the images appear to be symmetric along the long axis of the bone. Images are rotated so that this axis is parallel to the x axis. By assuming cylindrical symmetry, we reduce diffusion calculations to a one-dimensional problem given by

$$\frac{\partial C}{\partial t} = D\frac{\partial^2 C}{\partial x^2} + \frac{\partial D}{\partial x}\frac{\partial C}{\partial x} - v\frac{\partial C}{\partial x}. \quad (3)$$

Time series of tracer entry into the cartilage consisting of 100 images at 5.8 s intervals are collected directly after IC injection. These images are simplified to 100 curves by averaging image data laterally across the growth plate. As evident from Fig. 4 *d*, the raw data contains ''sharp'' features, high frequency pixel-to-pixel variations, due either to photon shot noise or cellularly resolved structures within the growth plate. Such features cause selection of artifactual D and v values. Fifth-order polynomial fits to these curves provided smoothed fits to the curves, while allowing fast calculations of first and second (spatial) derivatives. All image analysis was accomplished using algorithms written within the IDL scripting language (Research Systems, Boulder, CO). To limit the analysis to significant changes in tracer signal, only curves from 30 to 180 s after IC injection are analyzed. At each point in each curve in this dataset, the time rate of change of the fluorescence as well as its first and second derivatives with respect to the long axis are calculated. D and v values are chosen via minimization of the χ-square value (33) at each axial position,

$$\chi^2 = \sum \frac{\left[\frac{\partial C}{\partial t} - \left(D\frac{\partial^2 C}{\partial x^2} + \frac{\partial D}{\partial x}\frac{\partial C}{\partial x} - v\frac{\partial C}{\partial x}\right)\right]^2}{\sigma^2/n}, \quad (4)$$

where the sum is over data from different time points, σ^2 is the variance of measured $\partial C/\partial t$ values calculated laterally along the growth plate, and n is the number of lines averaged. For all data analyzed, χ^2 values averaged to 2.1. For each series analyzed, we chose three points along the growth plate and plotted the χ^2 surface. The χ^2 minimization displayed as a trough with an average width of $\Delta D = 11\ \mu m^2/s$ and $\Delta v = 0.48\ \mu m/s$, so that the error due to the χ^2 convergence was significantly smaller than that due to experimental variation (see Results). This image analysis method for determining D and v transport coefficients was tested and verified using both simulated images of molecular diffusion and image data from 1-mm-wide channels with FL and 40k-FL (Fig. 2). The calculated D and v curves from individual growth plates were compared and averaged by normalizing the x axis such that the epiphyseal COJ is 0.0 and the metaphyseal COJ is 1.0.

RESULTS

Ex vivo matrix diffusion properties

To understand the transport properties of growth plate cartilage, we initially examined the diffusional properties of isolated tibial sections using MP-FPR. Fluorescence photobleaching traces were acquired several cell-layers-deep in cartilage sections incubated with fluorescently labeled probes of three different molecular sizes. Measurements were taken at ~20-μm intervals from the E to the M ends of the cartilage (marked by *squares* in the representative ovalbumin-FL incubated specimen in Fig. 3 *a*). Fig. 3 *b* shows two representative photobleaching traces (*red* and *orange*) in the proliferative and hypertrophic zones of the growth plate, respectively. Representative data along the growth plate is plotted in Fig. 3 *c* as a function of the normalized growth plate distance diagramed in Fig. 1. For this specimen, diffusion coefficients at the E and M COJs were 40% and 60% less than the peak value at the axial center of the growth plate. This same trend is consistent with general data from FL (*blue*, $n = 7$), 10k-FL (*green*, an anionic dextran, $n = 6$), and Ova-FL (*yellow*, a neutral 45 kDa protein, $n = 6$) plotted in Fig. 3 *d*. Using MP-FPR in solution, diffusion coefficients for FL, 10k-FL, and Ova-FL were 265 ± 30, 88 ± 10, and 55 ± 8 $\mu m^2/s$, respectively. These measurements generally conform to a Stokes-Einstein hard sphere analysis, in which the viscous drag is determined by the inverse radius of the molecule, and are consistent with values in the literature (34). Measured D-values in cartilage are also consistent with this model; for example, diffusion coefficients for the FL and the 10k-FL vary by roughly threefold, the ratio one calculates for a $(MW)^{-1/3}$ dependence. (The measured ratio is more precisely 2.5-fold, presumably reflecting the fact that FL is a planar molecule.)

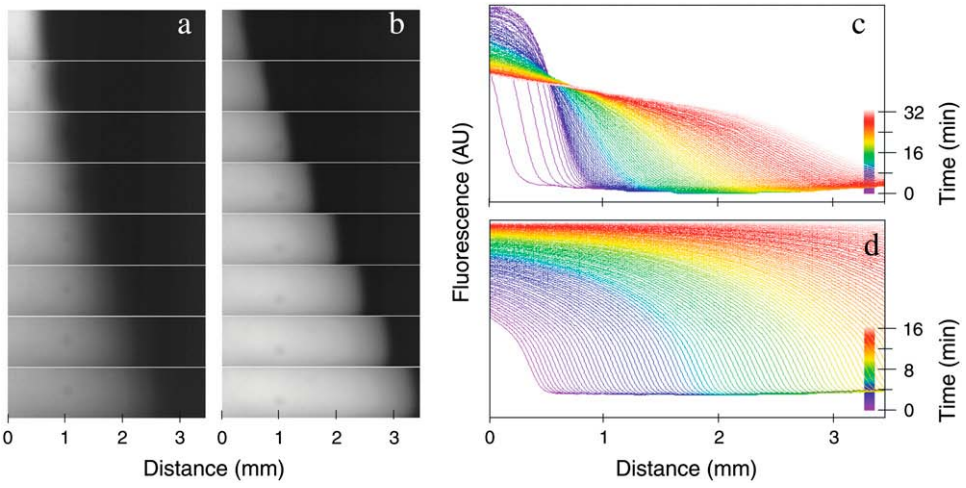

FIGURE 2 Verification of our image-based method for measuring diffusion. Images of (*a*) FL and (*b*) 40k-FL diffusing in a 1-mm-wide channel with flow. Images are acquired at 10-s intervals but displayed at 200 and 100 s intervals for FL and 40k-FL, respectively. To avoid edge effects, only data from the center of the channel were used. Fluorescence data from the FL and 40k-FL time series were averaged laterally across the channel and displayed in curves that are color-coded to indicate time (*c* and *d*, respectively). Note that at these temporal and spatial scales, FL transport is dominated by diffusion, which tends to equilibrate concentration gradients, but 40k-FL transport is dominated by flow, which causes a translocation of concentration gradients. Fits to the curves yielded average diffusion (flow) values of 223 $\mu m^2/s$ (2.3 $\mu m/s$) and 56 $\mu m^2/s$ (4.2 $\mu m/s$) for FL and 40k-FL, respectively. Solution diffusion coefficients were within 30% of those measured using standard FPR measurements described subsequently and those reported in the literature (51). Multiphoton images were acquired as described in Materials and Methods, except that a low magnification 4×/0.28 NA Olympus macro objective was used for obtaining the necessary large field-of-view.

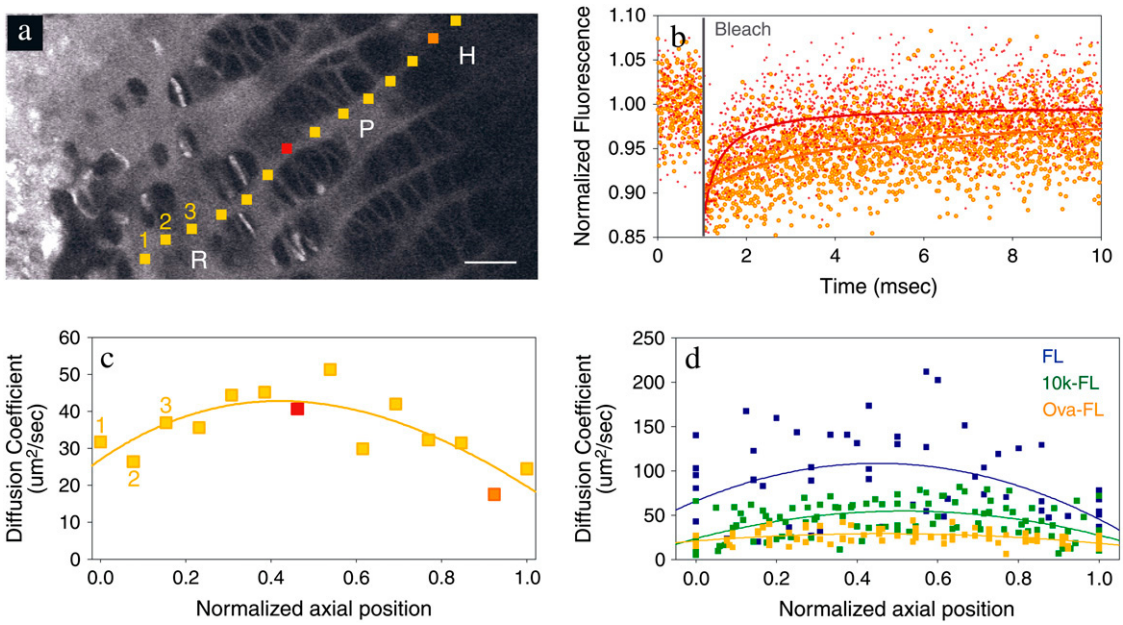

FIGURE 3 Multiphoton fluorescence photobleaching recovery diffusion measurements. Proximal tibial sections are isolated, sectioned once midsagitally, and incubated in either FL, 10k-FL or Ova-FL. (*a–c*) Representative data from an Ova-FL incubated growth plate. Scale bar = 25 μm. The laser is parked at the locations indicated (*squares*) and a 50-μs pulse bleaches out ~20% of the fluorescence in the focal spot; the timescale of fluorescence recovery is fit to determine diffusion coefficients for the species in that location. Example FPR traces from the red and orange squares are shown in panel *b* with their respective fits. (*c*) Diffusion coefficients for the locations indicated in panel *a* are plotted against the normalized axial position along the growth plate. The curve shows a polynomial fit to the data. (*d*) Cumulative plot of data such as those in panel *c* from multiple experiments and multiple tracers. These data represent measurements from $n = 7$ (FL, *blue*), $n = 6$ (10k-FL, *green*), and $n = 6$ (Ova-FL, *yellow*) similar experiments.

In vivo transport properties of small molecules

Because of its ability to penetrate relatively deeply into optically scattering specimens, multiphoton microscopy offers a unique opportunity to visualize the growth plate in vivo. Direct imaging in the living animal allows us to account for transport characteristics within the environment of an intact growth plate, which experiences a wide spectrum of physiologic pressures and potentially interstitial fluid flow due to an intact circulatory system. We cannot measure diffusion coefficients using MP-FPR in an intact growth plate primarily because we are unable to achieve the powers necessary for photobleaching the dye after penetrating through the perichondrium. (Other problems with this method in vivo include flow and breathing artifacts.) Our approach in the living animal has been to administer a bolus of fluorescent tracer to the circulatory system via an intracardiac injection and directly observe fluorescent tracer movement into the growth plate region. We previously showed that fluorescent tracers of 10,000 MW and less saturate the full growth plate region (~300 μm across) within 5 min (29).

Representative data of vascular fluorescein extravasating and moving into the ECM of a growth plate is shown in the time series of images 18, 54, and 102 s after the IC injection (Fig. 4, *a–c*). The fluorescence intensity is averaged laterally across the growth plate to generate the time series of fluorescence profiles in Fig. 4 *d*, color-coded to indicate time. Initial fits using diffusion as the only transport parameter yielded abnormally high diffusion coefficients and inconsistent fits. We found that fitting the tracer equilibration data for both diffusion and flow (convection) transport processes was essential for achieving consistent results. To fit the data, the laterally averaged fluorescence (Fig. 4 *d*) between the two COJs (demarcated by *dotted lines*) was fit to easily differentiated functions (*fifth-order polynomials*, Fig. 4 *e*). The rate of change of the data was then analyzed as a function of its first and second spatial derivatives for determining the local transport coefficients within the cartilage (Eq. 3). D and v curves were selected by a χ^2-minimization routine at each point along the growth plate (Eq. 4). To compare the transport coefficients of different growth plates, the axial position from all growth plates is normalized to 0.0 at the E COJ and 1.0 at the M COJ. The approximate positions of the resting, proliferative, and hypertrophic zones are diagramed for reference along this scale in Fig. 1. The blue and orange curves plotted in Fig. 4 *f* show axially specific diffusion coefficients and flow rates for the particular series shown in Fig. 4, *a–c*. The error bars show the average mean ± SE for $n = 7$ such series. Overall flow is directed from the two vascularized COJs into the cartilage. Diffusion coefficients are found to be fivefold higher in the axial center of the cartilage than at the two COJs. Note that at the metaphyseal COJ, a trough in the fluorescence intensity often appears over time (Fig. 4 *d*). This is a consistent result, which we believe is real and may result from lymphatic drainage within the region.

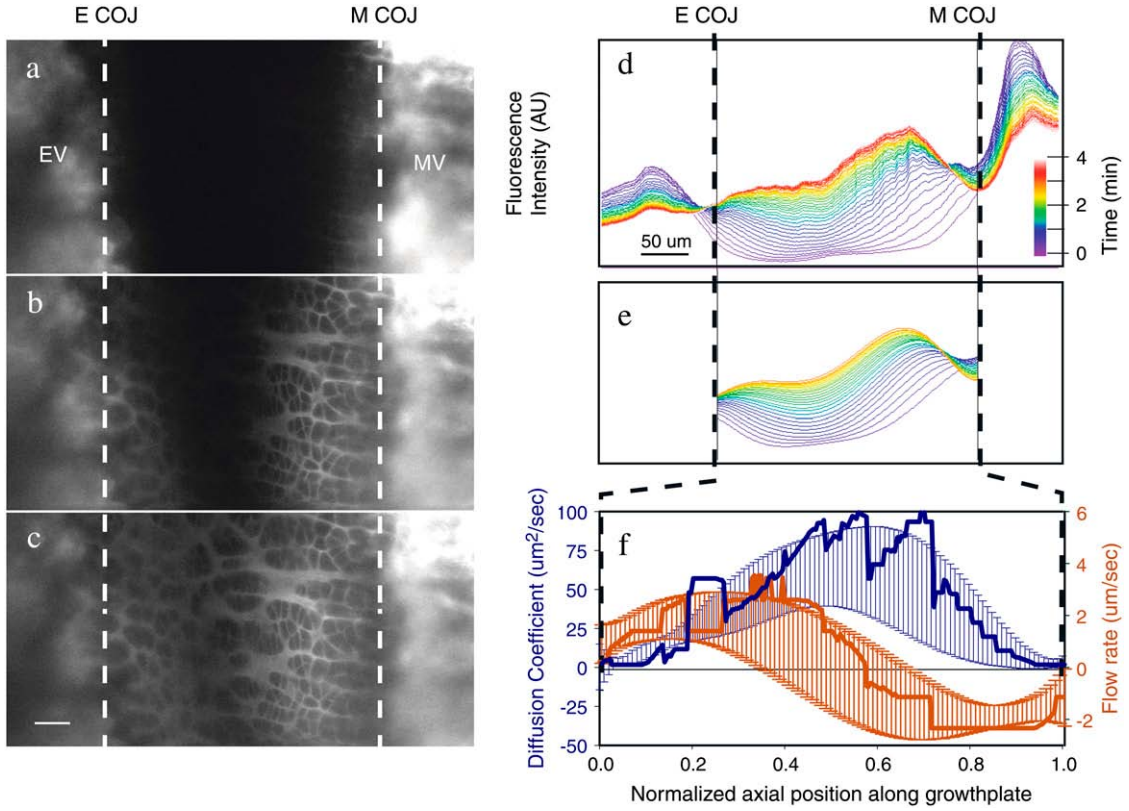

FIGURE 4 Multiphoton images of the proximal tibial growth plate 165-μm deep from the superficial surface of the perichondrium in a 32-day-old mouse (*a*) 18, (*b*) 54, and (*c*) 102 s after an IC injection of FL. The tracer is distributed to the epiphyseal and metaphyseal vasculature (*EV* and *MV*) within seconds and reaches the axial center of the growth plate within minutes (scale bar = 50 μm). Such images are recorded every 5.8 s and the intensity values are averaged laterally and displayed color-coded for time in panel *d*. Polynomial fits to these curves (*e*) provide functions that are smoothed and easily differentiable. Local flow rates and diffusion coefficients are calculated by analyzing the rate-of-change of the fluorescence and comparing it to the first and second spatial derivatives at every point. For comparison among growth plates, the axial position along the growth plate is normalized such that the *E* and *M* COJs are at 0.0 and 1.0, respectively; positions are demarcated by vertical dotted lines throughout the figure. (*f*) The blue and orange curves represent the local *D* and *v* values for the image series in panels *a–c*. The error bars show average mean ± SE for $n = 7$ similar experiments.

A caveat to this analysis is that differential partitioning of the tracer can occur within the growth plate due to binding and endocytosis, resulting in tracer that cannot move. The major problem seems to be fluorescence that is actively transported into the hypertrophic chondrocytes, resulting in a stronger signal from the hypertrophic region of the growth plate. This effect is especially visible after 5 min. We tried several methods for alleviating these effects, both normalizing to an ''equilibrated'' tracer concentration and masking out fluorescence inside the cells using thresholding algorithms. In both cases, extra complications were introduced to the analysis and the problems were not entirely alleviated. We decided instead to use a relatively fast analysis window; only data from 30 to 180 s after injection were analyzed. This time window maximized the effect of the real concentration differential due to the injection, while minimizing partitioning effects. Note that the concentration maximum in the hypertrophic region (Fig. 4 *d*) moves in toward the axial center, an indication that it represents a translocation of the injection bolus as it flows across the growth plate rather than an effect due to differential partitioning.

Another caveat to this experiment is that although we image deep enough into the growth plate that chondrocytic columns are parallel and aligned perpendicular to the two COJs, we are still toward the edge of the bone. For instance, Fig. 4, *a–c*, shows images that are 165-μm deep (through 90 μm of perichondrium and 75 μm of growth plate). However, tibias in mice this age average 1.2 mm in width, so we are still only imaging within the outer quarter of the growth plate; results must be interpreted accordingly.

In vivo transport properties of larger molecules

We previously showed that FL as well as the larger fluoresceinated dextrans enter the growth plate from three primary vascular sources, the epiphyseal and metaphyseal vasculature as well as the circumferential plexus surrounding the growth plate. Compared quantitatively to the amount of FL entering the region, 3 kDa and 10 kDa dextrans only enter the growth plate at 62 and 15%, respectively (29). Though all tracers can arrive from all three vascular sources, repeated imaging observations with different size indicators at the same region

in the same growth plate suggest a subtle difference in the arrival pattern; the larger and more anionic dextrans tend to arrive more from the subperichondrial plexus than does FL. For example, Fig. 5 *a* shows the edge of the growth plate, or the ''groove of Ranvier'', 63, 168, and 290 s after an IC injection of 10k-FL. Note that the larger tracer seems to arrive from the edge (*arrow*), presumably from the subperichondrial plexus encircling the cartilage disk. Note also that the 10k-FL never entirely equilibrates within this measurement window. Fig. 5 *b* shows the same region 12, 46, and 93 s after a second IC injection, this time with FL. In this series, the tracer arrived to the growth plate faster and clearly from the *E* and *M* vasculatures. We see this same trend toward a more circumferential entrance for the larger dextrans in five out of eight similar experiments. (The other three experiments were inconclusive due to a lack of signal in the growth plate.) Because of a combination of low signal and lack of axial symmetry in the entrance time series, the elemental image analysis protocol could not be used for determining transport coefficients for these larger tracers.

The more circumferential entrance of the larger dextrans occurs at least in part because of a severe transport block into the growth plate at the metaphyseal COJ. Fig. 6 *a* shows an image series at 90-s intervals after an IC injection of 10k-FL. Note that the tracer leaks out of the metaphyseal vasculature and labels the matrix of the primary spongiosa, but very little of it moves across the metaphyseal COJ and into the cartilage. A similar series after an IC injection of FL (at 12-s intervals, Fig. 6 *b*) shows the tracer quickly crossing the COJ boundary upon extravasating from the metaphyseal vasculature. In Fig. 6, *c* and *d*, fluorescence values from the vasculature (*red*), the bone matrix (*blue*), and the growth plate just adjacent to the COJ (*green*) are plotted as a function of time for the two series. Note that for 10k-FL (Fig. 6 *c*), fluorescence in the bone matrix peaks several minutes after that from the vasculature, but signal in the cartilage does not appreciably rise (remaining <0.1 of the peak vasculature signal). For the FL, however, all three regions have comparable intensities and all three regions peak within seconds after the cardiac injection, implying no transport barriers either across the metaphyseal vasculature or across the COJ. These types of observations are difficult to assess at the epiphyseal COJ, where the bone structure is more scattering to light and tends to obstruct the acquisition of clear images in this region. We have previously shown that 10k-FL ultimately reaches the growth plate at an amount that is 10-fold less than that of

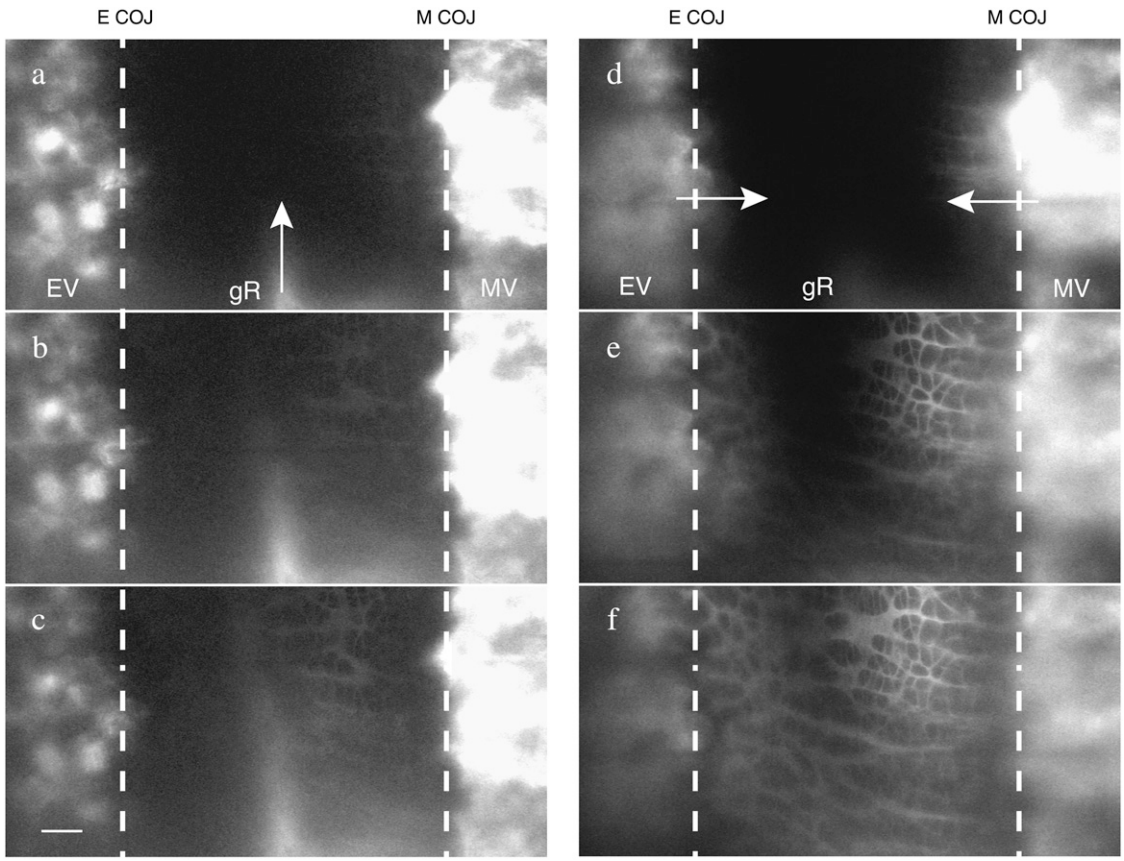

FIGURE 5 Arrival patterns of 10k-FL and FL at the same location. Multiphoton images of the growth plate edge, the ''groove of Ranvier'', acquired (*a*) 63, (*b*) 168, and (*c*) 290 s after an IC 10k-FL injection and (*d*) 12, (*e*) 46, and (*f*) 93 s after a second injection, this time with FL. Note that the 10k-FL exhibits a more circumferential arrival whereas the FL clearly enters from both bone vasculatures. Scale bar = 50 μm.

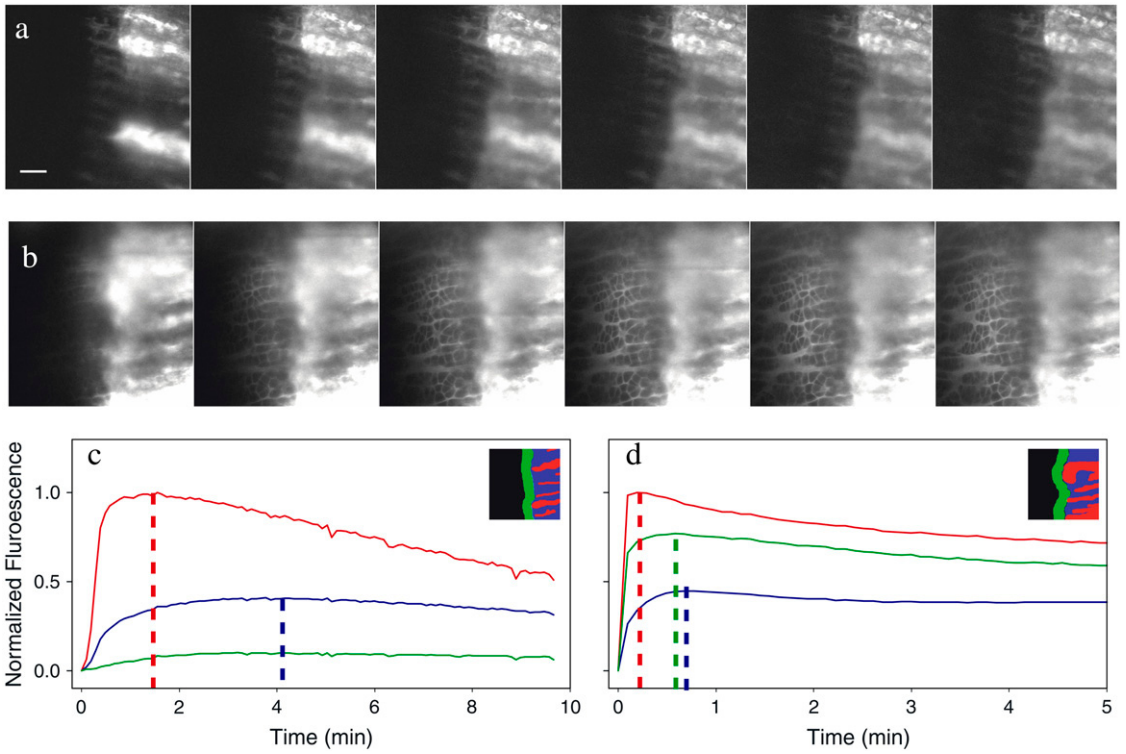

FIGURE 6 10k-FL transport is effectively blocked at the metaphaseal COJ. (*a*) Time series of images at 90 s intervals showing that the IC-injected 10k-FL leaks from the metaphyseal vasculature into the primary spongiosa, but not to an appreciable degree into the cartilage. (*b*) A similar series of images (12 s intervals) after a FL injection showing that FL immediately enters the cartilage as well. Scale bar = 50 μm. (*c*) Average intensity plotted as a function of time for the 10k-FL series in panel *a*. Different regions (the vasculature, the primary spongiosa, and the cartilage just adjacent to the metaphyseal COJ) are color-coded in red, blue, and green, respectively (see *inset*). Note that the fluorescence peaks at 90 s in the vasculature and in the spongiosa a few minutes later. The tracer does not significantly enter the cartilage. (*d*) A similar analysis of the FL-injected images shows that all regions peak within less than a minute.

FL (29). The transport block at the metaphyseal COJ appears to be the primary reason that the larger dextrans ($\geq$10 kDa) do not efficiently enter this region from the metaphyseal vasculature, not the permeability of the vasculature itself. Because we were unable to use neutral dextrans for this experiment (see Materials and Methods), we could not separate the effects of charge from those of size. However, the FL and 10k-FL diffusion coefficients were measured to be at most twofold different in the ex vivo experiments (Fig. 3 *d*), so we suspect that the transport block may be a charge effect.

DISCUSSION

Diffusion profile: zonal differences within the growth plate

Researchers have measured molecular diffusion in a wide variety of cartilage preparations (35–42). Cartilage measurements of small molecules (tetramethylrhodamine and sucrose (35,37,39,40), 10 kDa dextrans (35,37,39,40) and 40 kDa molecules (35–37,39) vary six-, four-, and 25-fold, respectively. Our measurements lie within these ranges. We know of only one diffusion measurement made in growth plate cartilage—a 66 kDa albumin in the proliferative zone of a porcine growth plate section was measured to be $D = 49$ $\mu m^2/s$ (41). Our own diffusion measurements are consistent, showing a smaller 45 kDa ova-FL in the proliferative zone of the mouse cartilage explant with D ranging from 30 to 50 $\mu m^2/s$. There has been no literature discussion of a transport gradient along the chondrocytic differentiation axis. Our measured diffusion profiles are presumably indicative of consistent changes in matrix structure along the growth plate axis.

Our results from in vivo and ex vivo FL diffusion measurements differ in several ways. Firstly, diffusion coefficients were measured to be two-to-threefold higher in the tissue sections than in the live animal (Fig. 3 *d* vs. Fig. 4 *f*). This difference may be due to the pressures encountered in cartilage with an intact perichondrium (43), effectively decreasing the fluid phase volume, which is expected to decrease diffusion twofold (38). Secondly, the decreasing gradient of diffusion values toward the *E* and *M* COJs is less pronounced in the tissue sections (twofold versus fivefold in the live animal). Whether the discrepancies between the in vivo and ex vivo measurements are real or due to experimental error is unknown. Certainly the pressure gradients expected to exist in the cartilage structures of live animals (44) are absent in the ex vivo tissue. Furthermore the ex vivo measurements

are point measurements within the extracellular matrix only, whereas the in vivo results average over both cellular and noncellular regions. Thus the measurements will differ in the fractional volume (ϕ) available for diffusion (extracellular volume/total volume), which varies significantly within the different zones of the growth plate. For instance, ϕ in the proliferative and hypertrophic zones for this age mice was measured to be 0.61 and 0.38, respectively (45). The effect of the chondrocytic exclusion can be estimated using Maxwell's effective medium permeability approximation for randomly dispersed spheres (46):

$$\frac{D}{D_{\text{soln}}} = \frac{2\phi}{3-\phi}.$$

Using this estimation, the measured in vivo diffusion coefficients should be reduced to 0.51 and 0.29 as compared to the ex vivo proliferative and hypertrophic values, respectively. These reduced values agree quite well with our results (Fig. 3 *d*, ex vivo and Fig. 4 *d*, in vivo). Discrepancies between the results may also arise from matrix degradation in the ex vivo tissue sections or potential imaging artifacts from decreased transmission of light by calcified regions around the COJs in the live animals. Nonetheless, similar diffusive trends were found using two very different measurement modalities, suggesting that the matrix in the proliferative and early hypertrophic zones is at least two-to-fivefold as permissive as that at the two COJs.

Not only does the volume of the extracellular matrix (ECM) vary along the growth plate, the structure of the ECM varies as well. For instance, in human rib, the collagen ultrastructure, as visualized by EM, changes dramatically along the growth plate axis (47) and would be expected to influence transport properties. The matrix adjacent to the metaphyseal COJ is partially calcified and thus particularly dense (48). An image analysis of EM micrographs (47) accounting for a 30% volume reduction due to fixation (49) reveals a fractional intrafibrillar volume (f) available for molecular diffusion in resting, proliferative, and hypertrophic zones to be 0.54, 0.82, and 0.36, respectively. The resulting diffusional hindrance can be estimated using the Mackie and Meares approximation (50), which accounts for a tortuosity increase due to a polymeric matrix:

$$\frac{D_{\text{soln}}}{D} = \left(\frac{2-f}{f}\right)^2.$$

This equation is derived assuming that the size of the diffusing molecules is small compared to that of the obstacles, which is thought to be true for proteins of MW $<$ 70,000 in cartilage (47,51,52), alleviating the need for theories accounting for more complex protein-matrix interactions (53). The Mackie and Meares approximation yields a diffusional hindrance of 7.1, 2.1, and 21 in the three regions, respectively, which fits somewhat quantitatively to the graph in Fig. 4 *f*, assuming an intrafibrillar viscosity that is 1.8-fold increased compared to our solution fluorescein measurement of 265 $\pm$ 30 $\mu m^2/s$.

The resting zone contains large radial/transverse fibers that fix the perichondrium into the epiphyseal bone (54). Within the proliferating zone, the fractional intrafibrillar volume is minimal. Throughout their development, chondrocytes secrete new matrix and upon doing so, construct an environment that ultimately defines their interactions with other cells. After secretion of more and more matrix and after swelling and thus reducing the available extracellular volume for diffusion, hypertrophic chondrocytes can no longer communicate as freely with the perichondrium, where many of the signaling molecules originate (Fig. 7). This self-constructed environment may then partially define their development toward hypertrophy as perichondrium-produced molecules such as BMP2, fibroblast growth factor 18, and PTHrP (4,6,9,12) may become concentrated at the more permissive proliferative/hypertrophic junction, the transition at which chondrocytes commit to hypertrophy. This low-collagen density region may represent a region where chondrocytes are particularly susceptible to lateral cross-talk between other chondrocytes and cells in the perichondrium. This permissive band is also evident in gadolinium-enhanced T1-weighted MR images of normal piglet hips (55), in which a dark band indicates a faster relaxation of tipped spins at the axial midplane of the growth plate.

In contrast at the metaphyseal COJ, the two extracellular proteins that are crucial to vascular invasion (and subsequent bone formation) are the angiogenic VEGFs and the ECM-degrading MMPs. These molecules tend to be tethered to cells or matrix elements. When both of these molecules are soluble and freely diffusing, the resulting vessel construction is nonviable, essentially with a bloated architecture. MMPs and VEGF must act in concert in a targeted mode of action for achieving a functional vessel architecture (56). In the case of the growth plate, vessels are organized such that each new vessel opposes the last transverse septum of the terminal hypertrophic chondrocyte of each column (57). At the metaphyseal COJ, it is primarily the matrix- and membrane-bound (nondiffusible) VEGF and MMP isoforms that are found to be crucial for targeted vascular invasion (13,16,22,58). MMP-9 is a diffusible protein that is involved in this process, but it is large (92 kDa) and relatively immobile with an estimated $<10\ \mu m^2/s$ diffusion. It is intriguing that at the metaphyseal COJ, where chondrocytes have already committed to differentiation and scaffolding for bone production has already been constructed, cellular interactions among chondrocytes, chondroclasts, and endothelial cells are conducted in a dense extracellular environment where cellular interactions are expected to be short range. By contrast, the matrix of the proliferating and early hypertrophic zones of the growth plate is relatively loose and permissive, allowing access to autocrine interactions between chondrocytes and paracrine interactions between chondrocytes and perichondrium-residing cells.

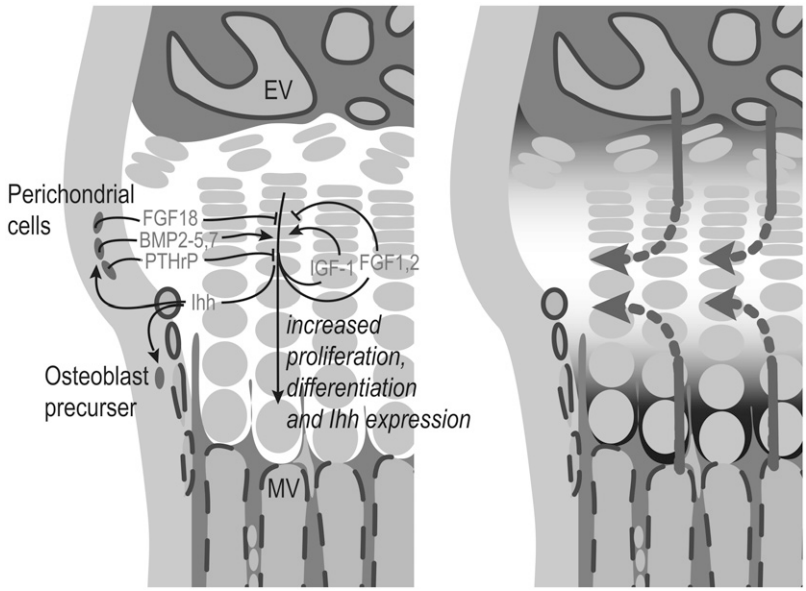

FIGURE 7 The illustration to the left displays transport routes critical to chondrocyte development and ultimately bone growth (4,6,9,12). To the right, hypothesized transport patterns within the growth plate are diagramed. Cartilage permissivity is coded by shading around the chondrocytes, with hindered diffusion near the two COJs. Axial flow measurements (*solid lines*) reveal flow that is directed away from the COJs. Draining toward the perichondrium is presumed (*dotted lines*). Note that due to both the heterogeneous diffusion characteristics and the overall flow profile, perichondrium-produced molecules will be enriched in the proliferative and early hypertrophic zones.

General transport patterns

In this study, we have confirmed our previous study (29) determining that FL tracer entry patterns (Fig. 4) show no indication of a proposed unidirectional entrance to the growth plate sourced by the epiphyseal vasculature. Though transport patterns are generally symmetric from both the *E* and *M* vasculatures, it is unknown whether the concentration of nutrients and oxygen within the two vasculatures are equivalent or whether the consumption of these molecules within the growth plate causes a differential availability to different populations of chondrocytes (59). Because tracers arrive to the two vasculatures within seconds after an IC injection, the former possibility seems improbable. The *E*-to-*M* asymmetry in vasculature-chondrocyte communication may ultimately stem from an as-yet unidentified diffusible survival signal from the *E* vasculature.

Fluid flow was found to contribute significantly to molecular transport of substances from the blood stream into the cartilage, implying a pressure differential between the bone vasculature and the cartilage matrix. Due to conservation of mass, this flow profile from the two COJs ultimately suggests an overall centrifugal flow toward the perichondrium (though a small percentage of the fluid would be shunted to hypertrophic swelling.) As a result, nutrients or hormones produced or released in the COJs would become distributed throughout the growth plate, but molecules produced or released in the perichondrium would tend to remain concentrated within the more permissive central cartilage canal. Such is in fact true for the 10k-FL transport pattern evident in Fig. 5, *a–c*. Note that Fig. 5 *c* was acquired almost 5 min after injection and still the tracer remains relatively concentrated adjacent to the subperichondrial plexus from which it originated. In contrast, FL, which tends to enter more from the two COJs, equilibrates through the growth plate within 90 s. (Note that the diffusion coefficient for 10k-FL is only twofold smaller than that for FL, implying only a twofold difference in equilibration times if transport in both cases were purely diffusive.) The overall centrifugal flow pattern is characteristic of a resting limb only; limb stresses and movement are expected to significantly alter cartilage pressure gradients.

Fig. 7 is a diagram of the growth plate demonstrating the three vascular access routes, and also indicating several molecules of biological significance thought to be active in autocrine and paracrine signaling pathways during the chondrocytic differentiation cascade. In the present study, we have used fluorescent tracers as surrogates for physiologically meaningful molecules, and all interpretations of the data have been made in terms of a combination of diffusion and flow within the growth plate's ECM. Our goal for this study was to establish a baseline understanding of transport in this region. Clearly, our model is a simplification of the in vivo situation. In the living animal specializations of the endothelial cells of each of the three access routes (including fenestrae, caveolae, transendothelial pores, cell-to-cell junctions, and specific receptors) may, in different combinations, either restrict or facilitate entrance of a particular biological molecule from a given vascular direction, and thus influence its pattern of distribution within the ECM (60). Furthermore, our tracers were chosen to be relatively biologically inert, whereas signaling molecules are not. Binding to ECM elements and cell surfaces in selected locations would significantly slow molecular transport. For example, the Ihh distribution was shown to be dramatically influenced by heparin sulfate chains on extracellular matrix proteoglycans (17–19). In addition, secreted molecules, such as IGF-1 or FGFs-1 or 2, might bind to the ECM and subsequently influence the same cell in an autocrine response later in the cell's life span. This would require no physical change in position of the molecule

itself within the ECM; time would, in effect, negate any requirement of movement, since the cell that originally synthesized the molecule could mature and subsequently react to it (61). An important point indicated in Fig. 7 and supported by our data is that a signaling molecule such as BMP-2, which is produced by cells within the perichondrium, will tend to accumulate at the relatively permissive proliferative/hypertrophic junction (Fig. 5 *a*) due to flow patterns that are generally directed away from the bone. In contrast, molecules that enter with equal facility from either the metaphyseal or the epiphyseal bone will become distributed throughout the growth plate (Fig. 5 *b*).

This research was performed in the Developmental Resource for Biophysical Imaging and Opto-Electronics and was made possible by grants R01AR052003-01 from National Institutes of Health/National Institute of Arthritis and Musculoskeletal and Skin Diseases and 9 P41 EB001976-16 from National Institutes of Health/National Institute of Biomedical Imaging and Bioengineering.

REFERENCES

1. Breur, G. J., B. A. VanEnkevort, C. E. Farnum, and N. J. Wilsman. 1991. Linear relationship between the volume of hypertrophic chondrocytes and the rate of longitudinal bone growth in growth plates. *J. Orthop. Res.* 9:348–359.
2. Hunziker, E. B., and R. K. Schenk. 1989. Physiological mechanisms adopted by chondrocytes in regulating longitudinal bone growth in rats. *J. Physiol.* 414:55–71.
3. Wilsman, N. J., C. E. Farnum, E. M. Leiferman, M. Fry, and C. Barreto. 1996. Differential growth by growth plates as a function of multiple parameters of chondrocytic kinetics. *J. Orthop. Res.* 14: 927–936.
4. Karsenty, G., and E. F. Wagner. 2002. Reaching a genetic and molecular understanding of skeletal development. *Dev. Cell.* 2:389–406.
5. Kornak, U., and S. Mundlos. 2003. Genetic disorders of the skeleton: a developmental approach. *Am. J. Hum. Genet.* 73:447–474.
6. Kronenberg, H. M. 2003. Developmental regulation of the growth plate. *Nature.* 423:332–336.
7. Ortega, N., D. J. Behonick, and Z. Werb. 2004. Matrix remodeling during endochondral ossification. *Trends Cell Biol.* 14:86–93.
8. Provot, S., and E. Schipani. 2005. Molecular mechanisms of endochondral bone development. *Biochem. Biophys. Res. Commun.* 328: 658–665.
9. van der Eerden, B. C., M. Karperien, and J. M. Wit. 2003. Systemic and local regulation of the growth plate. *Endocr. Rev.* 24:782–801.
10. Chung, U. I., E. Schipani, A. P. McMahon, and H. M. Kronenberg. 2001. Indian hedgehog couples chondrogenesis to osteogenesis in endochondral bone development. *J. Clin. Invest.* 107:295–304.
11. Vortkamp, A., K. Lee, B. Lanske, G. V. Segre, H. M. Kronenberg, and C. J. Tabin. 1996. Regulation of rate of cartilage differentiation by Indian hedgehog and PTH-related protein. *Science.* 273:613–622.
12. Ballock, R. T., and R. J. O'Keefe. 2003. The biology of the growth plate. *J. Bone Joint Surg. Am.* 85A:715–726.
13. Holmbeck, K., P. Bianco, J. Caterina, S. Yamada, M. Kromer, S. A. Kuznetsov, M. Mankani, P. G. Robey, A. R. Poole, I. Pidoux, J. M. Ward, and H. Birkedal-Hansen. 1999. MT1-MMP-deficient mice develop dwarfism, osteopenia, arthritis, and connective tissue disease due to inadequate collagen turnover. *Cell.* 99:81–92.
14. Holmbeck, K., P. Bianco, I. Pidoux, S. Inoue, R. C. Billinghurst, W. Wu, K. Chrysovergis, S. Yamada, H. Birkedal-Hansen, and A. R. Poole. 2005. The metalloproteinase MT1-MMP is required for normal development and maintenance of osteocyte processes in bone. *J. Cell Sci.* 118:147–156.
15. Vu, T. H., J. M. Shipley, G. Bergers, J. E. Berger, J. A. Helms, D. Hanahan, S. D. Shapiro, R. M. Senior, and Z. Werb. 1998. MMP-9/gelatinase B is a key regulator of growth plate angiogenesis and apoptosis of hypertrophic chondrocytes. *Cell.* 93:411–422.
16. Zhou, Z., S. S. Apte, R. Soininen, R. Cao, G. Y. Baaklini, R. W. Rauser, J. Wang, Y. Cao, and K. Tryggvason. 2000. Impaired endochondral ossification and angiogenesis in mice deficient in membrane-type matrix metalloproteinase I. *Proc. Natl. Acad. Sci. USA.* 97:4052–4057.
17. Hilton, M. J., L. Gutierrez, D. A. Martinez, and D. E. Wells. 2005. EXT1 regulates chondrocyte proliferation and differentiation during endochondral bone development. *Bone.* 36:379–386.
18. Koziel, L., M. Kunath, O. G. Kelly, and A. Vortkamp. 2004. Ext1-dependent heparan sulfate regulates the range of Ihh signaling during endochondral ossification. *Dev. Cell.* 6:801–813.
19. The, I., Y. Bellaiche, and N. Perrimon. 1999. Hedgehog movement is regulated through tout velu-dependent synthesis of a heparan sulfate proteoglycan. *Mol. Cell.* 4:633–639.
20. Mizutani, C. M., Q. Nie, F. Y. Wan, Y. T. Zhang, P. Vilmos, R. Sousa-Neves, E. Bier, J. L. Marsh, and A. D. Lander. 2005. Formation of the BMP activity gradient in the *Drosophila* embryo. *Dev. Cell.* 8:915–924.
21. Trueta, J. 1968. Studies of the Development and Decay of the Human Frame. William Heinemann Medical Books, London.
22. Maes, C., I. Stockmans, K. Moermans, R. Van Looveren, N. Smets, P. Carmeliet, R. Bouillon, and G. Carmeliet. 2004. Soluble VEGF isoforms are essential for establishing epiphyseal vascularization and regulating chondrocyte development and survival. *J. Clin. Invest.* 113:188–199.
23. Shapiro, I. M., K. D. Mansfield, S. M. Evans, E. M. Lord, and C. J. Koch. 1997. Chondrocytes in the endochondral growth cartilage are not hypoxic. *Am. J. Physiol.* 272:C1134–C1143.
24. Schipani, E. 2005. Hypoxia and HIF-1α in chondrogenesis. *Semin. Cell Dev. Biol.* 16:539–546.
25. Ham, K. N., J. V. Hurley, G. B. Ryan, and E. Storey. 1965. Localization of particulate carbon in metaphyseal vessels of growing rats. *Aust. J. Exp. Biol. Med. Sci.* 43:625–638.
26. Brown, E. B., E. S. Wu, W. Zipfel, and W. W. Webb. 1999. Measurement of molecular diffusion in solution by multiphoton fluorescence photobleaching recovery. *Biophys. J.* 77:2837–2849.
27. Zipfel, W. R., and W. W. Webb. 2001. In vivo diffusion measurements using multiphoton excited fluorescence photobleaching recovery (MPFPR) and fluorescence correlation spectroscopy (MPFCS). *In* Methods in Cellular Imaging. A. Periasamy, editor. Oxford University Press, Oxford, UK.
28. Zipfel, W. R., R. M. Williams, and W. W. Webb. 2003. Nonlinear magic: multiphoton microscopy in the biosciences. *Nat. Biotechnol.* 21:1369–1377.
29. Farnum, C. E., M. Lenox, W. Zipfel, W. Horton, and R. Williams. 2006. In vivo delivery of fluoresceinated dextrans to the murine growth plate: imaging of three vascular routes by multiphoton microscopy. *Anat. Rec. A Discov. Mol. Cell. Evol. Biol.* 288:91–103.
30. Xu, C., and W. W. Webb. 1996. Measurement of two-photon excitation cross sections of molecular fluorophores with data from 690 to 1050 nm. *J. Opt. Soc. Am. B.* 13:481–491.
31. Zipfel, W. R., R. M. Williams, R. Christie, A. Y. Nikitin, B. T. Hyman, and W. W. Webb. 2003. Live tissue intrinsic emission microscopy using multiphoton-excited native fluorescence and second harmonic generation. *Proc. Natl. Acad. Sci. USA.* 100:7075–7080.
32. Crank, J. 1975. The Mathematics of Diffusion. Clarendon Press, Oxford.
33. Bevington, P. R. 2003. Data Reduction and Error Analysis for the Physical Sciences. McGraw-Hill, Boston.
34. Atkins, P. 1994. Physical Chemistry. W. H. Freeman and Company, New York.
35. Boubriak, O. A., J. P. Urban, S. Akhtar, K. M. Meek, and A. J. Bron. 2000. The effect of hydration and matrix composition on solute diffusion in rabbit sclera. *Exp. Eye Res.* 71:503–514.

36. Leddy, H. A., and F. Guilak. 2003. Site-specific molecular diffusion in articular cartilage measured using fluorescence recovery after photobleaching. *Ann. Biomed. Eng.* 31:753–760.

37. Maroudas, A. 1970. Distribution and diffusion of solutes in articular cartilage. *Biophys. J.* 10:365–379.

38. Nimer, E., R. Schneiderman, and A. Maroudas. 2003. Diffusion and partition of solutes in cartilage under static load. *Biophys. Chem.* 106:125–146.

39. Quinn, T. M., P. Kocian, and J. J. Meister. 2000. Static compression is associated with decreased diffusivity of dextrans in cartilage explants. *Arch. Biochem. Biophys.* 384:327–334.

40. Quinn, T. M., V. Morel, and J. J. Meister. 2001. Static compression of articular cartilage can reduce solute diffusivity and partitioning: implications for the chondrocyte biological response. *J. Biomech.* 34:1463–1469.

41. Sniekers, Y. H., and C. C. van Donkelaar. 2005. Determining diffusion coefficients in inhomogeneous tissues using fluorescence recovery after photobleaching. *Biophys. J.* 89:1302–1307.

42. Torzilli, P. A., J. M. Arduino, J. D. Gregory, and M. Bansal. 1997. Effect of proteoglycan removal on solute mobility in articular cartilage. *J. Biomech.* 30:895–902.

43. Wong, M., and D. R. Carter. 2003. Articular cartilage functional histomorphology and mechanobiology: a research perspective. *Bone.* 33:1–13.

44. Grodzinsky, A. J., M. E. Levenston, M. Jin, and E. H. Frank. 2000. Cartilage tissue remodeling in response to mechanical forces. *Annu. Rev. Biomed. Eng.* 2:691–713.

45. Bailon-Plaza, A., A. O. Lee, E. C. Veson, C. E. Farnum, and M. C. van der Meulen. 1999. BMP-5 deficiency alters chondrocytic activity in the mouse proximal tibial growth plate. *Bone.* 24:211–216.

46. Cussler, E. 1984. Diffusion: Mass Transfer in Fluid Systems. Cambridge University Press, Cambridge.

47. Keene, D. R., J. T. Oxford, and N. P. Morris. 1995. Ultrastructural localization of collagen types II, IX, and XI in the growth plate of human rib and fetal bovine epiphyseal cartilage: type XI collagen is restricted to thin fibrils. *J. Histochem. Cytochem.* 43:967–979.

48. Hunziker, E. B., and W. Herrmann. 1990. Ultrastructure of cartilage. *In* Ultrastructure of Skeletal Tissues. E. Bonucci and P. M. Motta, editors. Kluwer Academic Publishers, Norwell, MA.

49. Richards, R. G., and M. J. Kaab. 1996. Microwave-enhanced fixation of rabbit articular cartilage. *J. Microsc.* 181:269–276.

50. Mackie, J., and P. Meares. 1955. The diffusion of electrolytes in a cation-exchange resin membrane. *Proc. R. Soc. Lond. A.* 232:498–509.

51. Guiot, E., M. Enescu, B. Arrio, G. Johannin, G. Roger, S. Tosti, F. Tfibel, F. Merola, A. Brun, P. Georges, and M. P. Fontaine-Aupart. 2000. Molecular dynamics of biological probes by fluorescence correlation microscopy with two-photon excitation. *J. Fluoresc.* 10: 413–419.

52. Ramanujan, S., A. Pluen, T. D. McKee, E. B. Brown, Y. Boucher, and R. K. Jain. 2002. Diffusion and convection in collagen gels: implications for transport in the tumor interstitium. *Biophys. J.* 83: 1650–1660.

53. Pluen, A., P. A. Netti, R. K. Jain, and D. A. Berk. 1999. Diffusion of macromolecules in agarose gels: comparison of linear and globular configurations. *Biophys. J.* 77:542–552.

54. Speer, D. P. 1989. The growth plate: structure and function. *In* Principles of Orthopedic Practice. R. Dee, E. Mango, and L. C. Hurst, editors. McGraw-Hill, New York.

55. Jaramillo, D., S. A. Connolly, S. Vajapeyam, R. L. Robertson, P. S. Dunning, R. V. Mulkern, A. Hayward, S. E. Maier, and F. Shapiro. 2003. Normal and ischemic epiphysis of the femur: diffusion MR imaging study in piglets. *Radiology.* 227:825–832.

56. Lee, S., S. M. Jilani, G. V. Nikolova, D. Carpizo, and M. L. Iruela-Arispe. 2005. Processing of VEGF-A by matrix metalloproteinases regulates bioavailability and vascular patterning in tumors. *J. Cell Biol.* 169:681–691.

57. Farnum, C. E., and N. J. Wilsman. 1989. Cellular turnover at the chondro-osseous junction of growth plate cartilage: analysis by serial sections at the light microscopical level. *J. Orthop. Res.* 7:654–666.

58. Zelzer, E., W. McLean, Y. S. Ng, N. Fukai, A. M. Reginato, S. Lovejoy, P. A. D'Amore, and B. R. Olsen. 2002. Skeletal defects in VEGF(120/120) mice reveal multiple roles for VEGF in skeletogenesis. *Development.* 129:1893–1904.

59. Grunhagen, T., G. Wilde, D. M. Soukane, S. A. Shirazi-Adl, and J. P. Urban. 2006. Nutrient supply and intervertebral disc metabolism. *J. Bone Joint Surg. Am.* 88(Suppl 2):30–35.

60. Olsson, A. K., A. Dimberg, J. Kreuger, and L. Claesson-Welsh. 2006. VEGF receptor signaling—in control of vascular function. *Nat. Rev. Mol. Cell Biol.* 7:359–371.

61. Re, R. N., and J. L. Cook. 2006. An intracrine view of angiogenesis. *Bioessays.* 28:943–953.